

## Supporting Information

### **Highly Synergistic, Electromechanical and Mechanochromic Dual-Sensing Ionic Skin with Multiple Monitoring, Antibacterial, Self-healing, and Anti-freezing Functions**

Long Bai,<sup>a,b</sup> Yong Jin,<sup>\*a,b</sup> Xiang Shang,<sup>a,b</sup> Hongyu Jin,<sup>c</sup> Yutang Zhou,<sup>a,b</sup> and Liangjie Shi<sup>a,b</sup>

<sup>a</sup>. National Engineering Research Center of Clean Technology in Leather Industry, Sichuan University, Chengdu 610065, P.R. China.

<sup>b</sup>. Key Laboratory of Leather Chemistry and Engineering of Ministry of Education, Sichuan University, Chengdu 610065, P.R. China

<sup>c</sup>. Department of Liver Surgery & Liver Transplantation, State Key Laboratory of Biotherapy and Cancer Center, West China Hospital, Sichuan University and Collaborative Innovation Center of Biotherapy, Chengdu, China

\*Correspondence to: [jinyong@cioc.ac.cn](mailto:jinyong@cioc.ac.cn) (Yong Jin)

## **This material includes:**

### **1. Experimental section**

### **2. Supporting Figures**

**Figure S1.** Photographs of the cholesteric liquid crystals for pure H-HPC.

**Figure S2.** POM images of MFIHs with different content of  $Al^{3+}$  ions.

**Figure S3.** Effect of  $Al^{3+}$  ions content on the color of MFIHs.

**Figure S4.** SEM surfaces image and Mapping images of MFIHs with 4.0%  $Al^{3+}$  ions.

**Figure S5.** Mechanical properties of MFIH prepared with different content of  $Al^{3+}$  ions.

**Figure S6.** Lab values of MFIHs with changes of elongations and pressures.

**Figure S7.** Relationships between the resistances and length, width and thickness of MFIHs.

**Figure S8.** Changes of relative resistance and reflection wavelength during the cyclic tests.

**Figure S9.** Optical images of the yellow and green DSI-skins attached to forefinger used to monitor the bending motion by the changes of structural color.

**Figure S10.** Tensile stress–strain curves of DSI-skins with the different healing times.

**Figure S11.** Freezing resistance of DSI-skins.

**Figure S12.** DSI-skins based on  $Zn^{2+}$  ions.

**Figure S13.** Water-retention of DSI-skin.

**Figure S14.** Bright field, fluorescence, and merged images of L929 incubated with MIFH with 4.0%  $Al^{3+}$  ions and 4.0%  $Zn^{2+}$  ions.

**Figure S15.** Cytotoxicity of the extracts of MIFH against the L929 cell after incubating for 24 h.

**Figure S16.** Test angle of our mechanochronic sensor.

**Figure S17.** Mechanochromic sensing performance with temperature variation.

**Figure S18.** Electromechanical sensing performance with temperature variation.

### **3. Supporting Tables**

**Table S1.** Mechanical properties of the current structure color materials and artificial skins.

**Table S2.** Summary of representative humidity sensors.

**Table S3.** Comparison between DSI-skins and previously reported ion skins, photonic sensors or ionic hydrogels in terms of visual signal, electrical signal, antibacterial, self-healing and anti-freezing functions.

**Table S4.** Performances of our DSI-skin sensor compared with the previous studies regarding multifunctional hydrogel sensors.

**Table S5.** Novelties of our work compared with the other flexible sensors with electrical and visual dual-sensing functions.

### **4. Supporting References**

### **5. Supporting Movie**

**Movie S1.** Mechanochromic performance of stretching.

**Movie S2.** Mechanochromic performance of compressing.

**Movie S3.** Human motion detection by mechanochromic sensing function.

**Movie S4.** Human motion detection by electromechanical sensing function.

**Movie S5.** Respiratory detection.

**Movie S6.** Self-Healing function of MIFHs.

**Movie S7.** Human motion detection of healing DSI-skins.

**Movie S8.** Anti-freezing function of DSI-skins.

**Movie S9.** DSI-skins based on  $\text{Zn}^{2+}$  ions.

## 1. Materials and Methods

**Materials:** Aluminum chloride hexahydrate ( $\text{AlCl}_3 \cdot 6\text{H}_2\text{O}$ ) was supplied by Chengdu Kelong Chemical Co., Ltd. AAm was purchased from Beijing Balinwei Technology Co., Ltd. (S)-(-)-2-Amino-4-pentenoic acid (APA) was supplied by Shanghai McLean Biochemical Technology Co., Ltd. H-HPC (Degree of hydroxypropyl substitution: 74.1%; Viscosity = 4.8 mPa·s;  $M_w = 100000$ ) was bought from Nippon Soda Co., Ltd. 2-Hydroxy-4'-(2-hydroxyethoxy)-2-methylpropiophenone was supplied by Tixie (Shanghai) Chemical Industrial Development Co., Ltd. Sodium hydroxide was bought from Chengdu Jinshan Chemical Reagent Co. Ltd. The VHB tape (M3998) was bought from 3M Corporation. Double-distilled water was used in the preparation of MFIHs.

**Preparation of the MFIHs:** The MFIH was prepared by integrating the ionic hydrogel containing  $\text{Al}^{3+}$  ions with H-HPC. In detail, 1.08 g APA was reacted with 0.144 g NaOH in an aqueous solution. After the reaction, 0.72 g AAm and a certain content of  $\text{AlCl}_3 \cdot 6\text{H}_2\text{O}$  (0, 1.0, 2.0, 2.5, 3.0, 3.5, and 4.0 wt%) were added into the above mixture solution. The dose of  $\text{AlCl}_3 \cdot 6\text{H}_2\text{O}$  could be programmatically controlled as needed for the desired color and performance. In order to obtain structural color, 6.72 g H-HPC was gradually added and mixed for two days at ambient temperatures. Then, a 60  $\mu\text{L}$  photoinitiator was added, and the mixture was stirred a few days, away from light. The aforementioned mixture was degassed by the high-speed centrifuge (10k rpm, KL05A), and then poured into the tailored mold (polymethyl methacrylate, 40 mm  $\times$  30 mm  $\times$  1 mm (l  $\times$  w  $\times$  h)). After finishing self-assembly without light, the mold was placed on a UV light source (CEL-LB70). The MFIHs were obtained by polymerizing under UV light with wavelengths of 365 nm and an intensity of 8.0  $\text{W cm}^{-2}$  for over 30 min. The surface of MFIHs were coated with a thin layer of vaseline to avoid water evaporation before each test.

**Characterization of the MFIHs:** Universal ART Sampling Accessory (FT-IR/NIR Spectrometer 3, PerkinElmer) was used to analyze the coordination bonds between Al<sup>3+</sup> ions and carboxylate groups in the MFIHs. The liquid crystals phase of MFIHs were observed using polarized optical microscopy (POM, LEICA-DMLP 1, Leica Microsystems). The morphology of the MFIH was observed using a scanning electron microscope (SEM, Helios G4 UC, Thermo Fisher SCIENTIFIC) at an acceleration voltage of 15 kV.

**Characterization of mechanochromic sensing performances:** Images of MFIHs with different colors were vertically taken by a digital camera on a black background under controlled pressures or tensile strains. Reflectivity spectra were measured with UV-vis reflective spectrometer (Lambda 1050+, PerkinElmer) in the vertical direction of the materials. In order to accurately characterize the difference of colors, the Lab value of different colors was tested by Spectrophotometer (CM-5, Konica Minolta) based on Commission International de l'Eclairage (CIE) chromaticity values.

**Characterization of electromechanical sensing performances:** The resistance of MFIHs was measured by an electrochemical workstation (PMC CH808A, Princeton Applied Research). The conductivity of samples can be acquired by the following Equation S1:

$$\delta = L/(R \times S) \quad (S1)$$

where  $\delta$  is the conductivity in mS cm<sup>-1</sup>; L represents the length of the MFIHs (cm); R is the resistance of the MFIHs ( $\Omega$ ); S refers to the cross-sectional area of the sample (cm<sup>2</sup>). The electrical signal sensing function of the ionic skins was also investigated by an electrochemical workstation and a computer-linked digital multimeter (MT-1820, Pro'skit). The real-time resistance changes of the ionic skins were recorded by a computer-linked digital multimeter under different stress, pressure, and humidity environment (humidity chamber with saturated solutions of different salts to regulate the relative humidity). The relative variations of resistance were calculated by the following Equation S2:

$$\Delta R/R_0 (\%) = (R - R_0)/R_0 (\%) \quad (\text{S2})$$

where  $R_0$  and  $R$  are the initial resistance and the real-time resistance after stretching or compressing or human movements, respectively. During all tests, a VHB tape was used to assist and allow for a better fit of DSI-skin to the skin. All human-related experiments were reviewed and permitted by the Ethical Committee of the West China Hospital of Sichuan University.

***Mechanical tensile and self-healing properties test:*** Mechanical properties of the MFIHs were performed by electronic universal tests (Gotech, AI-7000SN) at room temperature, setting parameters with a 50 N load force and a constant 10 mm min<sup>-1</sup> tensile speed. The samples were tailored into a dumbbell shape (30mm × 4mm × 1mm (l × w × t)) meeting with tensile measurement. The self-healing properties of the MFIHs were measured by placing two cutting samples together at room temperature. The self-healing process was observed by optical microscopy (NOVEL OPTICS BM2000, NINGBO YONGXIN OPTICS CO., LTD) at different times. The electronic universal tester was employed to estimate the efficiency of self-heal. The self-healing efficiency of strain ( $\varepsilon\%$ ) and self-healing efficiency of stress ( $l\%$ ) can be calculated using the following Equations S3 and S4. Besides, the switching on/off of the circuit was also used to testify the self-repair of the MFIHs by showing the illumination and silence of LED before and after healing. During several cutting/healing cycles, the changes of current were recorded by a multifunction digital multimeter.

$$\varepsilon\% = (\varepsilon/\varepsilon_0) \times 100\% \quad (\text{S3})$$

where,  $\varepsilon$  is the tensile strength of the healed samples and  $\varepsilon_0$  represents the tensile strength of the pristine hydrogels.

$$l\% = (l/l_0) \times 100\% \quad (\text{S4})$$

where,  $l$  is the elongation of the healed samples,  $l_0$  refers to the elongation of the pristine hydrogels at the break.

**Antibacterial properties tests:** According to the prior method (Chem. Eng. J. 2019, 370, 1228), the surface antibacterial activity of MIFHs against *E. coli* and *S. aureus* was performed. In brief, 0.2 g of MIFHs were put into sterile test tubes respectively. Then, 20  $\mu\text{L}$  of bacterial suspension with  $10^6$  CFU  $\text{mL}^{-1}$  was added onto the surface of each MIFHs in the sterile test tube. The above MIFHs were incubated for 2 h at 37  $^{\circ}\text{C}$  in the thermostatic incubator (MJ-60, Shanghai Yuejin Medical Instrument Co., Ltd). At the end of that time, 980  $\mu\text{L}$  of sterilized culture medium was poured into each well to repeatedly re-suspend any surviving bacterial survivor. The 20  $\mu\text{L}$  of bacterial suspension with  $10^6$  CFU  $\text{mL}^{-1}$  diluted in 980  $\mu\text{L}$  of sterilized culture medium was served as a negative control. The 200  $\mu\text{L}$  bacterial suspension of each sample was inoculated onto an agar plate respectively. After incubated for 18 h at 37  $^{\circ}\text{C}$ , the colony-forming units (CFU) were counted and tests were repeated three times for each group. The antibacterial ability was evaluated by log reduction, which was computed by the following Equation S5:

$$\log \text{reduction} = \log(\text{cell count of negative control}) - \log(\text{survivor count of samples}) \quad (\text{S5})$$

**Anti-freezing properties tests:** The samples are placed in a  $-15$   $^{\circ}\text{C}$  refrigerator overnight. Subsequently, the samples are put on an ice block for measurement. All measurements are completed in three minutes. The differential scanning calorimetry (DSC 214 Polyma, NETZSCH) was employed to analyze the anti-icing performances of pure PASCA hydrogel and the MFIHs with different content of  $\text{Al}^{3+}$  ions, ranging from 25  $^{\circ}\text{C}$  to  $-50$   $^{\circ}\text{C}$  at a cooling rate of 5  $^{\circ}\text{C} \text{ min}^{-1}$ .

**Cytotoxicity tests:** The cytotoxicity evaluation of MIFH with 4.0%  $\text{Al}^{3+}$  ions or 4.0%  $\text{Zn}^{2+}$  ions was measured readily according to a reported method (Chem. Eng. J. 2019, 370, 1228). In brief, L929 cells were cultured in a normal medium (Dulbecco's modified Eagle's medium (DMEM) containing 10 % fetal bovine serum (FBS) and 1% penicillin-streptomycin solution) in an incubator (5%  $\text{CO}_2$  and 37  $^{\circ}\text{C}$ ). The cell proliferation and viability of L929 cells after exposure to MIFH extract solution were assessed using live/dead viability/Cell Counting Kit-8 (CCK-8) kit assay. The prepared cylindrical MIFHs (10 mm in length and 10



mm in diameter) were soaked in PBS to reach full swelling about 30min and then sterilized by autoclaving. Then, 1 g of the sample was extracted in a 5 mL normal medium at 37 °C for 24h. The cell culture medium was replaced with the MIFH extract solution. The cells were seeded into 96-well plates with a density of  $5 \times 10^4$  cells per well. After incubation for 24 h, the medium was replaced by a fresh medium containing the MIFHs extract solution, and L929 cells were incubated for 24 h. To observe the cell survival situation, the L929 cells were dyed with 4',6'-diamidino-2-phenylindole (DAPI) and propidium iodide (PI) ( $5 \mu\text{g mL}^{-1}$ ,  $100 \mu\text{L}$  per well) for 15 min at 37 °C. Last, and the cells were observed using an inverted fluorescence microscope (Nikon, Japan). A 10 vol% CCK-8 solution was directly added to each well for another incubation time of 1.5 h. The optical density (OD) was measured at 450 nm by a microplate reader (Tecan Infinite 200 PRO, Switzerland). The cell viability (CV) was calculated according to the following Equation S6:

$$\text{Cell viability} = \frac{\text{OD}_{\text{sample}}}{\text{OD}_{\text{control}}} \times 100\% \quad (\text{S6})$$

where,  $\text{OD}_{\text{control}}$  is the OD value of the control group and  $\text{OD}_{\text{sample}}$  is the OD value of experimental groups, respectively. All measurements were repeated five times and the average results were used.

## 2. Supporting Figures

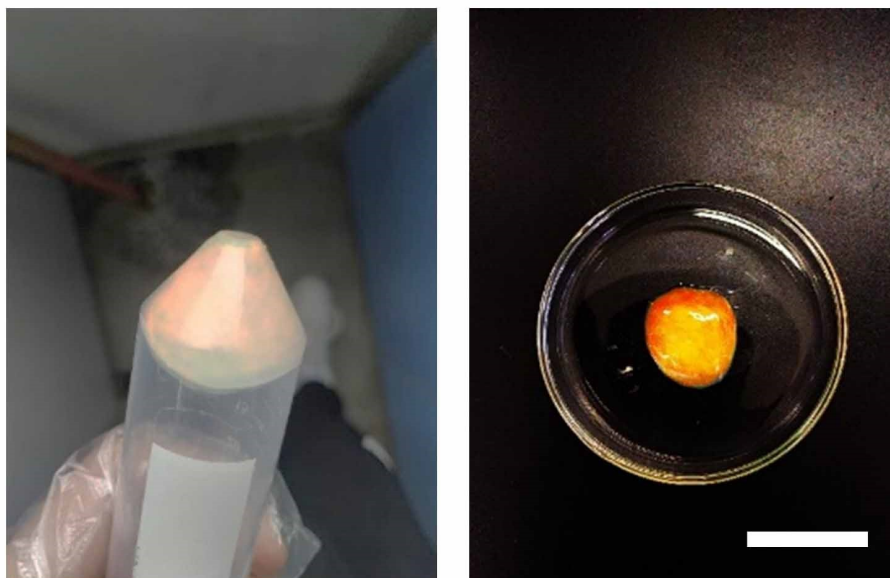


**Figure S1.** Photographs of the cholesteric liquid crystal for pure H-HPC; The scale bar is 2.0 cm.

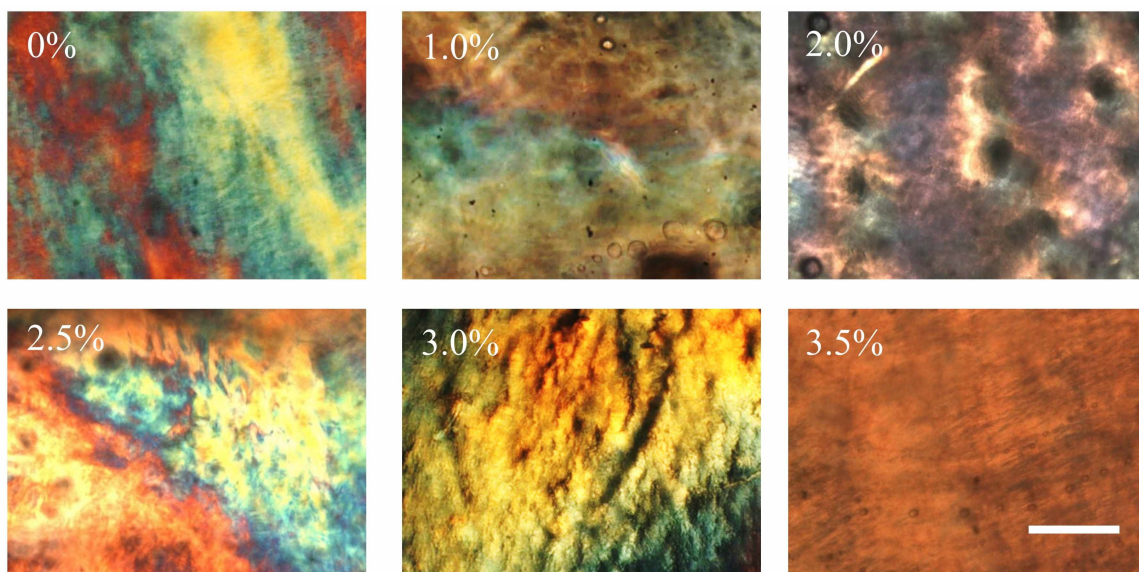


**Figure S2.** POM images of MFIHs with different content of Al<sup>3+</sup> ions; The scale bar is 500  $\mu\text{m}$ .

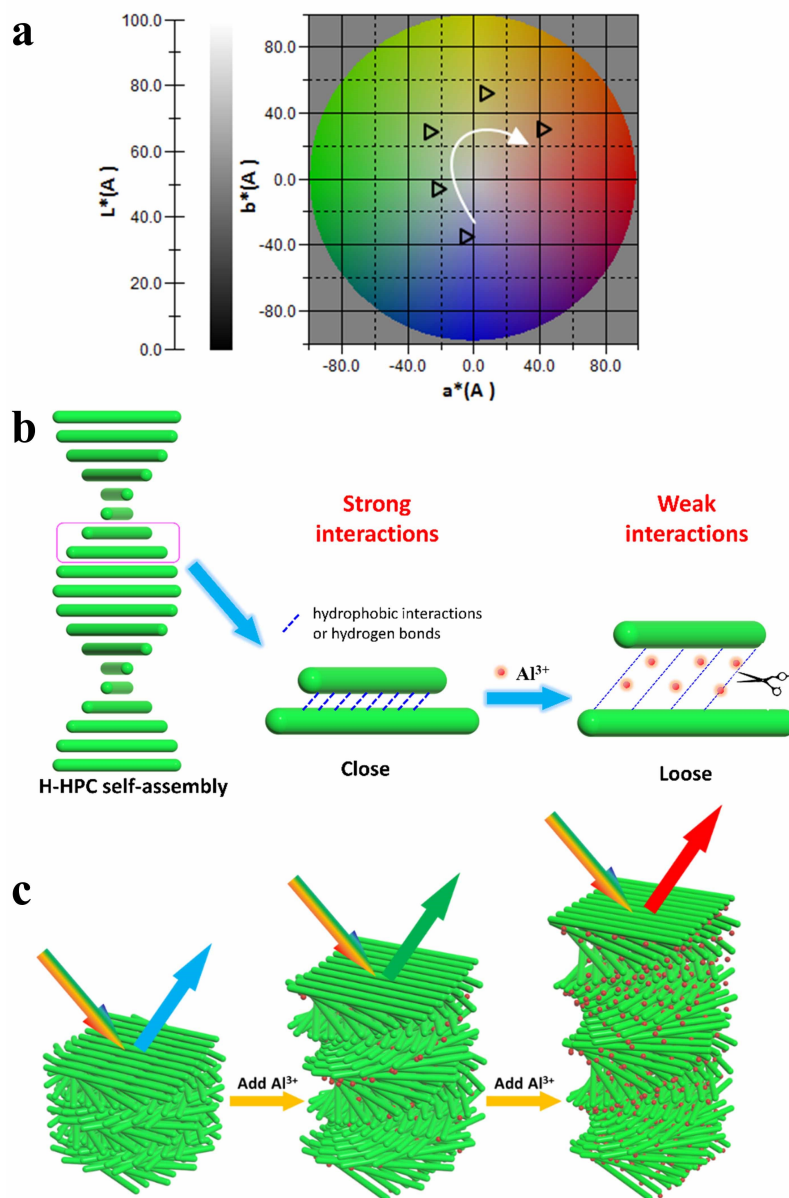


**Figure S3.** Effect of  $Al^{3+}$  ion content on the color of MFIHs. a) Lab values of MFIHs as a function of  $Al^{3+}$  ions content. b)  $Al^{3+}$  ions weakening the strength of the hydrophobic interactions and hydrogen bonds of H-HPC molecular chain. c) Mechanism illustration of color-switching with increasing of  $Al^{3+}$  content.

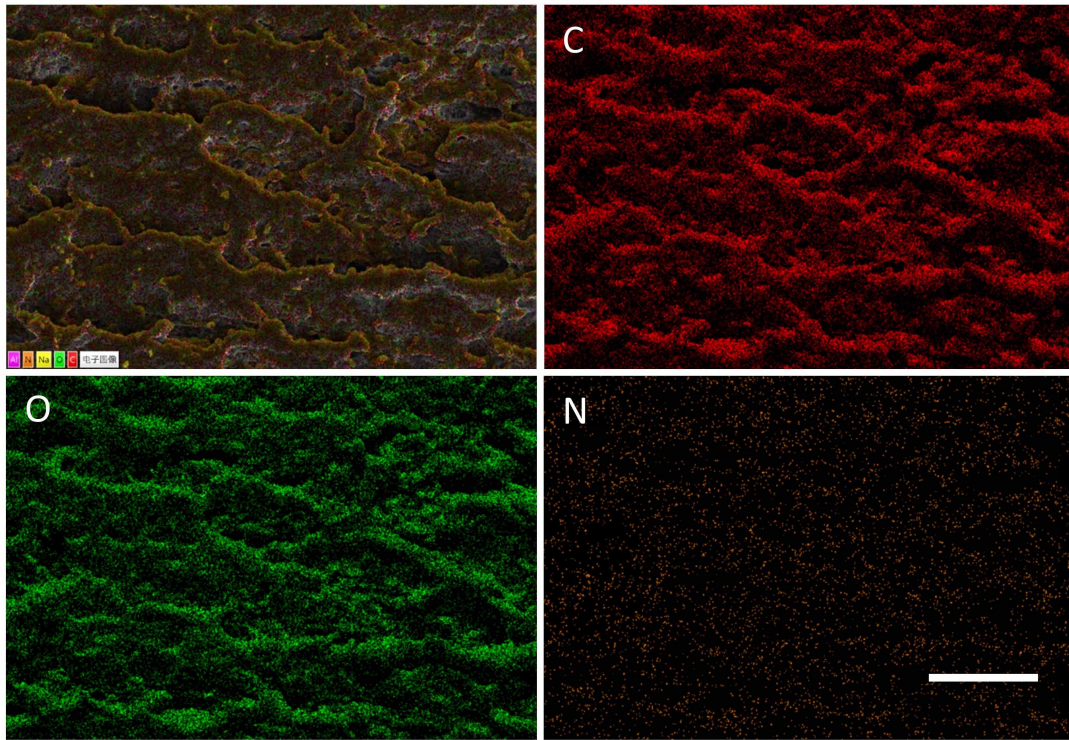


**Figure S4.** SEM surfaces image and mapping images of MFIHs with 4.0% Al<sup>3+</sup> ions; The scale bar is 50  $\mu\text{m}$ .

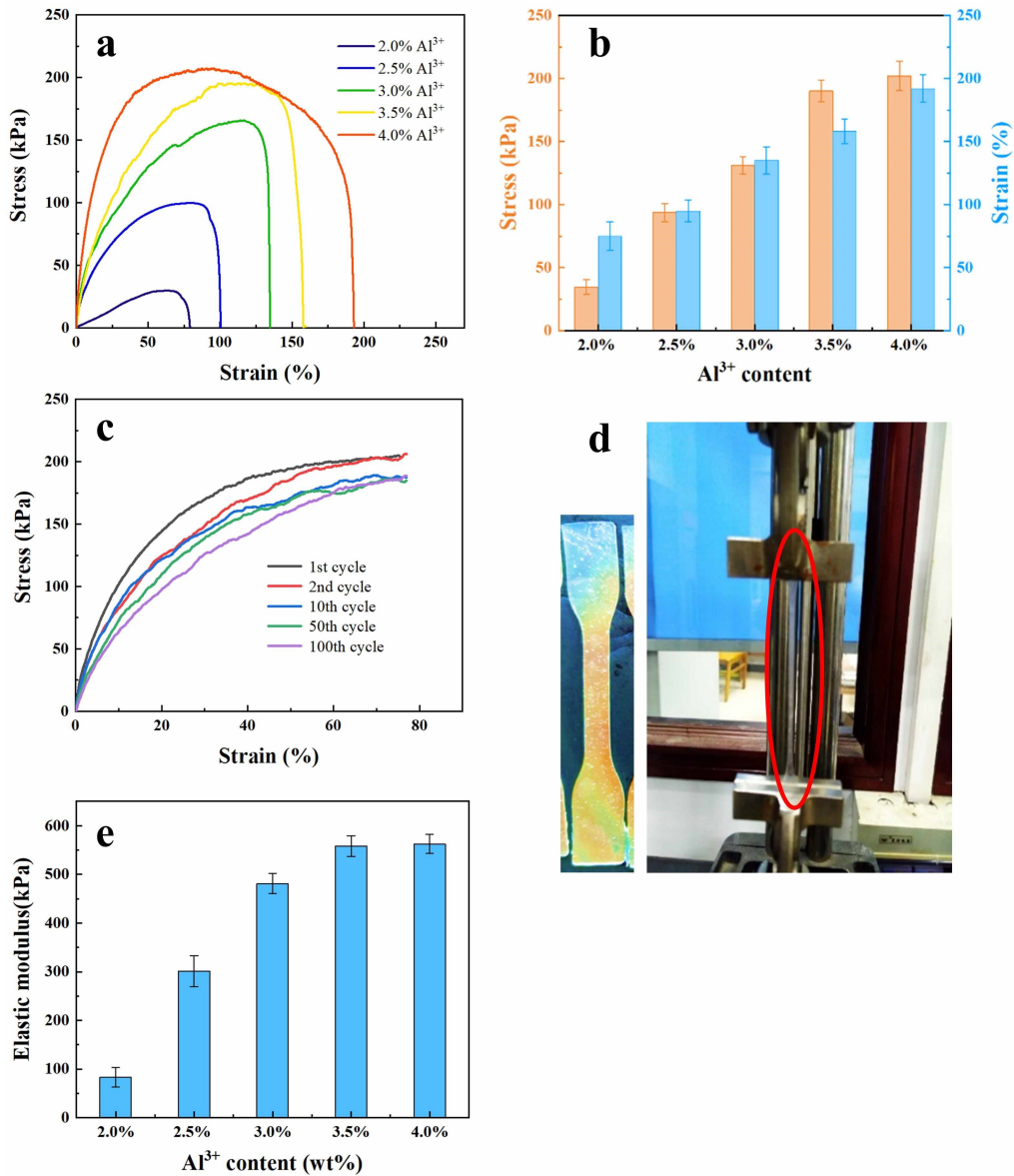


**Figure S5.** Mechanical properties of MFIHs prepared with different content of Al<sup>3+</sup> ions. a) Stress–strain curves. b) Stress and strain values. c) Repeated experiment of MFIH at 67% uniaxial tensile strain. d) Picture of tensile test. e) Elastic modulus.

The MFIHs prepared with 0% and 1.0% Al<sup>3+</sup> ions present the characteristics of viscous fluid and can not be shaped for the required test. Thus, they can not conduct test of the tensile machine.

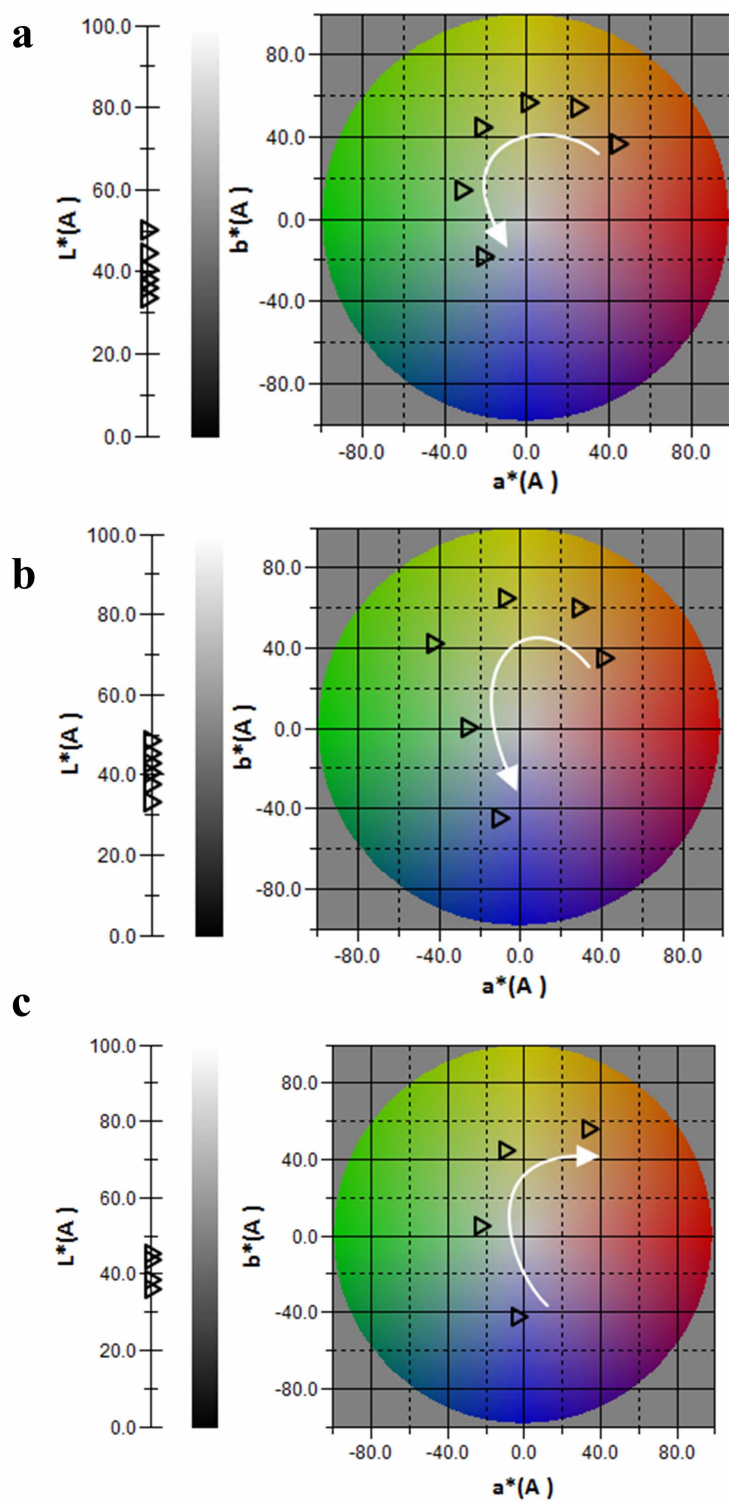


**Figure S6.** Lab values of MFIHs with change of 0~67% elongations a), 0~25kPa pressures b) and 30%~90% RH humidity.

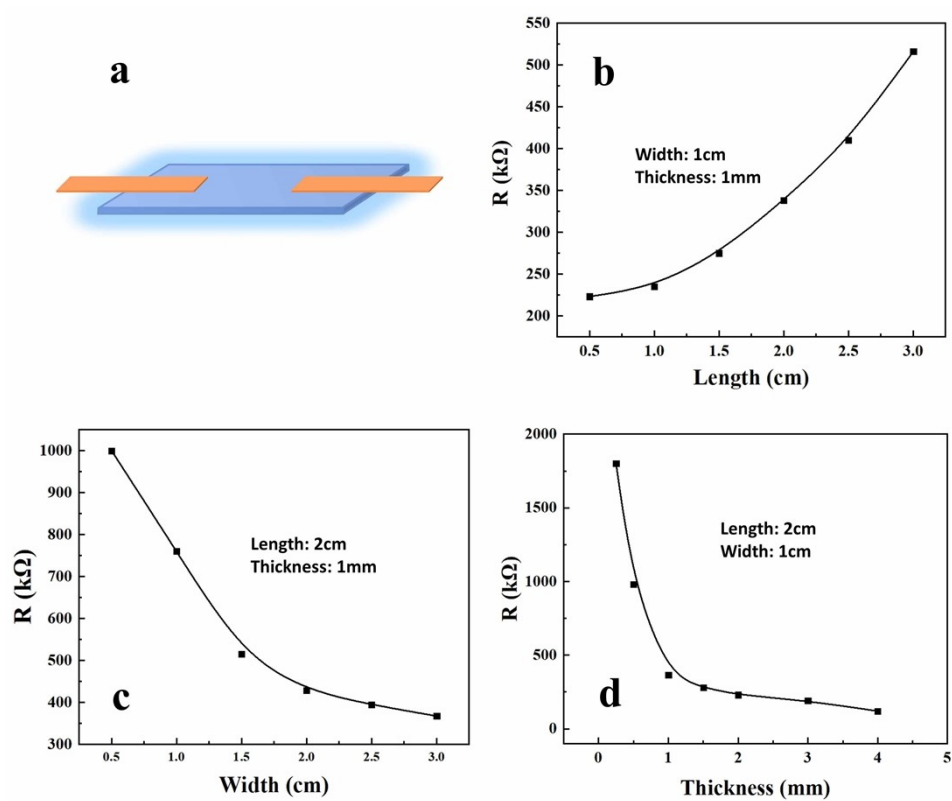


**Figure S7.** a) Optical image of the test for MFIHs resistance. Relationships between the resistance and b) length, c) width, d) thickness of MFIHs.



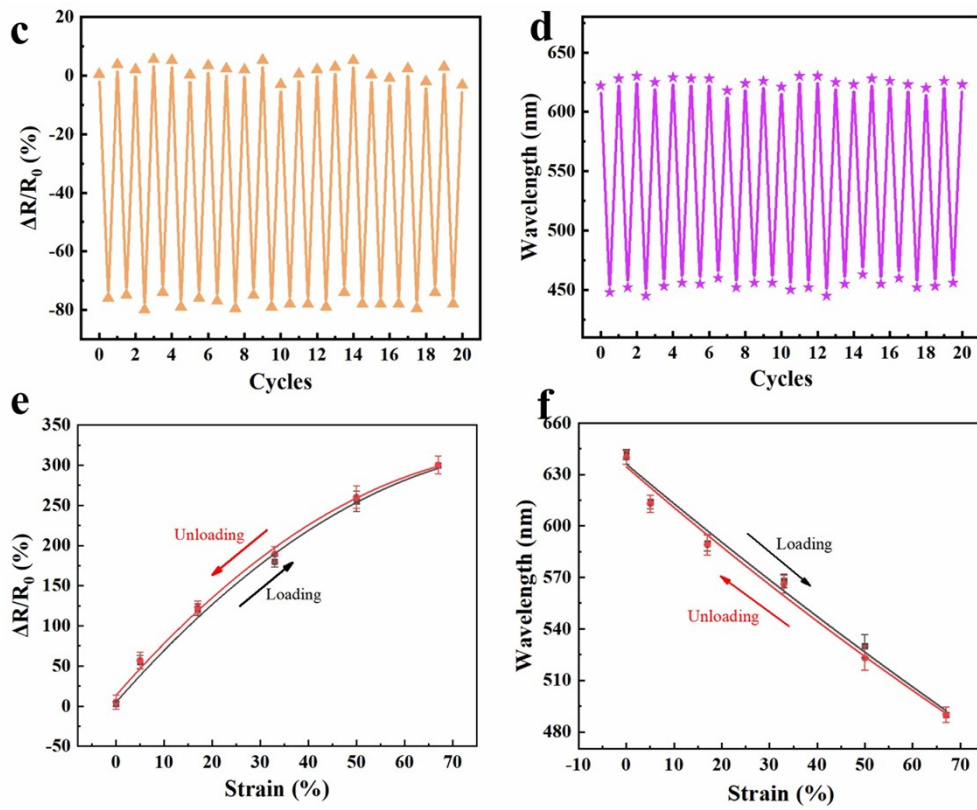


**Figure S8.** Changes of relative resistance and reflection peak during the cyclic tests. c) Relative resistance of MFIH under cyclic tests of pressure. d) Position of reflection peak of MFIHs under cyclic tests of pressure. e) Changes of relative resistance during loading-unloading cycles test within the strain ranges of 0% ~ 67%. f) Position of reflection peak during loading-unloading cycles test within the strain ranges of 0% ~ 67%.

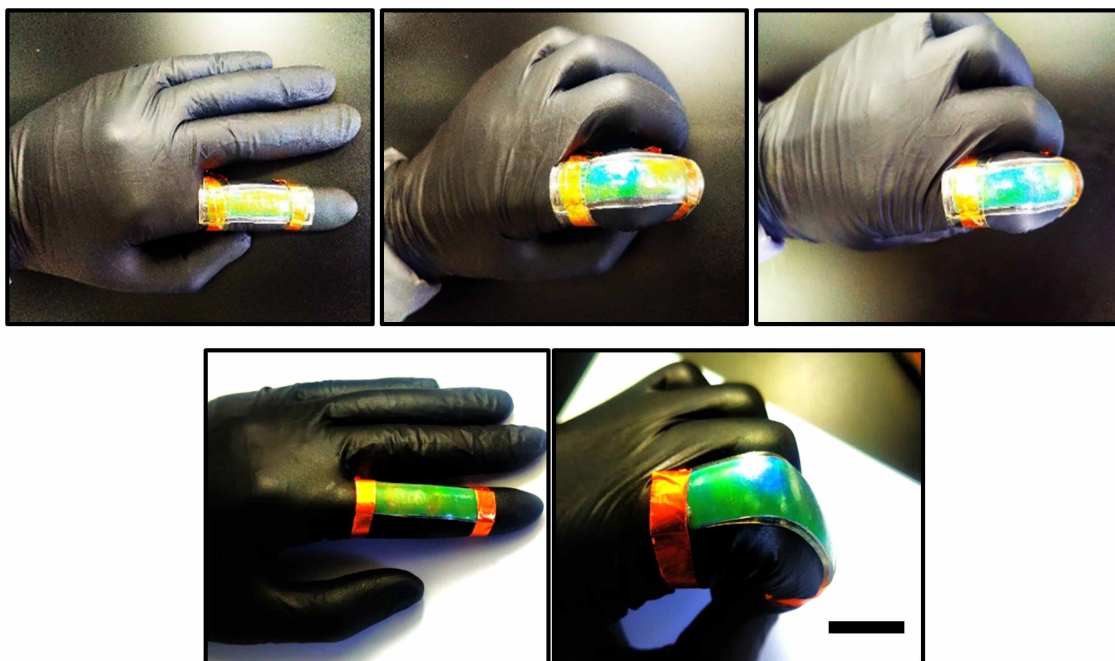


**Figure S9.** Optical images of the yellow and green DSI-skins attached to forefinger used to monitor the bending motion; The scale bar is 2.0 cm.

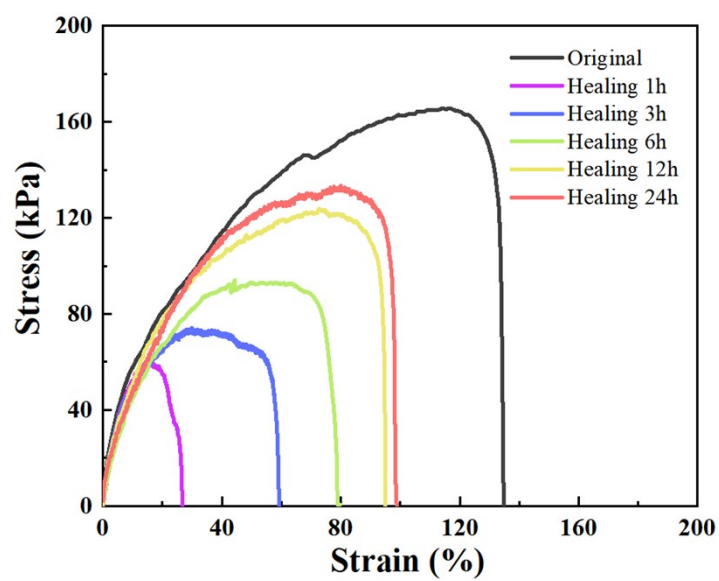


**Figure S10.** Tensile stress-strain curves of DSI-skins with the different healing times.

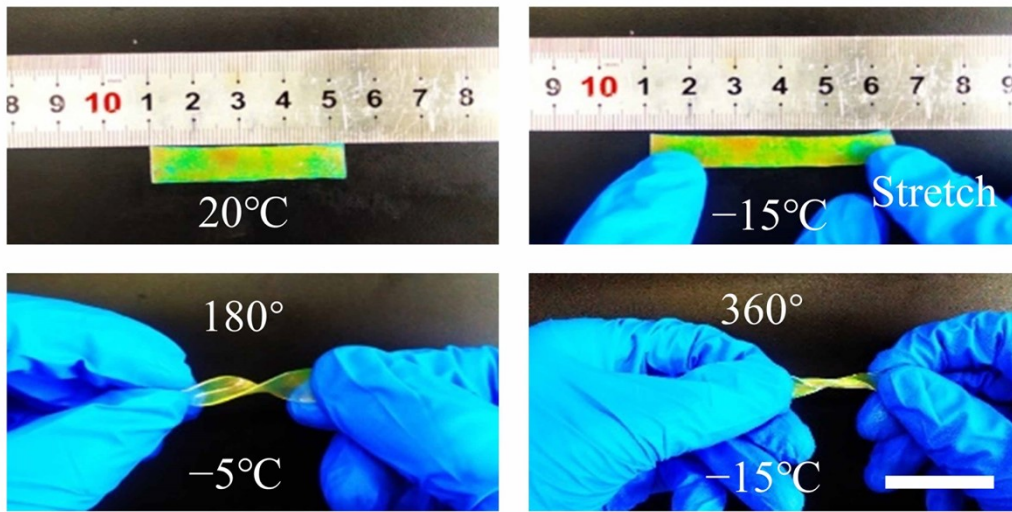


**Figure S11.** Freezing resistance of DSI-skins; The scale bar is 2.0 cm.

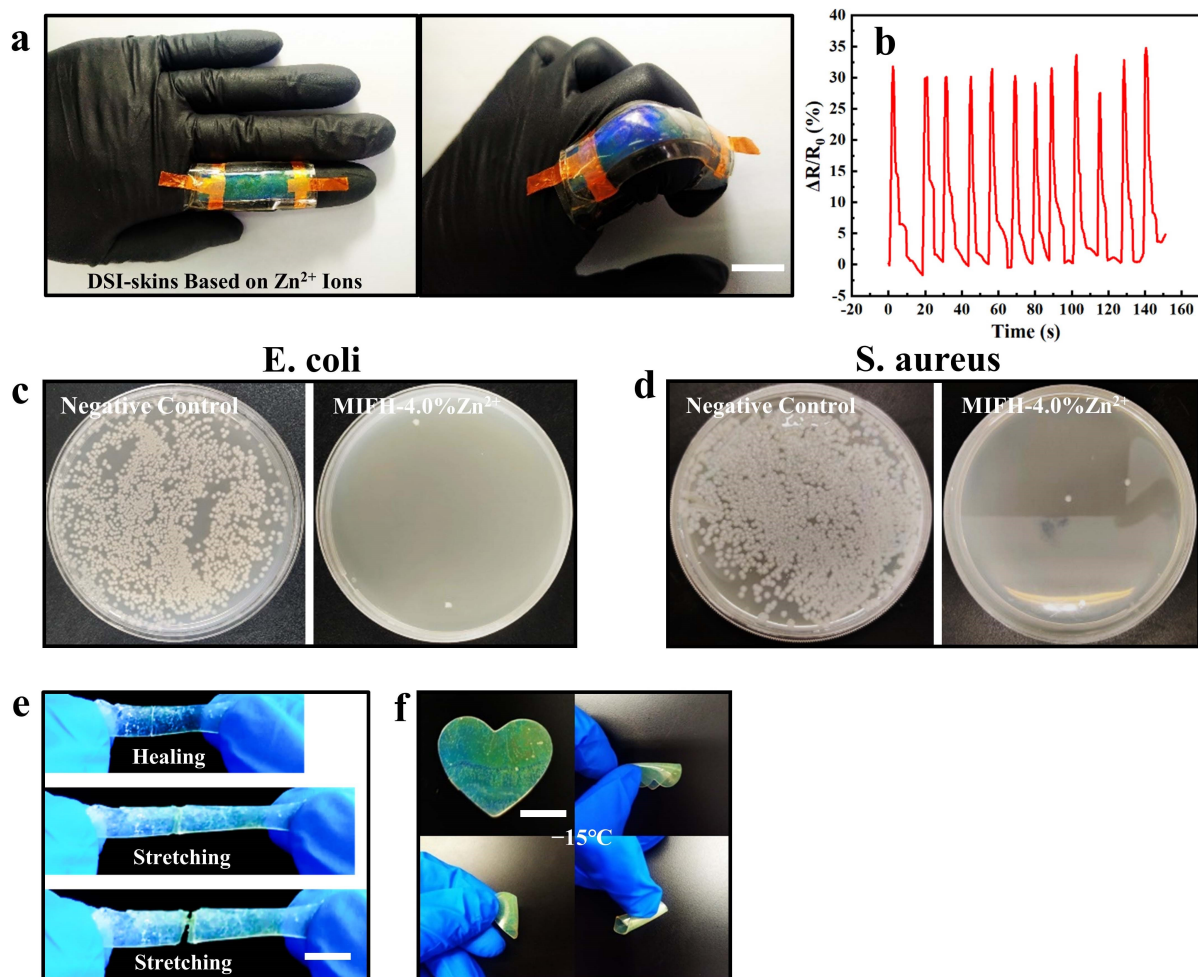


**Figure S12.** DSI-skins based on  $Zn^{2+}$  ions. (a) Mechanochromic sensing function of DSI-skin with 4.0%  $Zn^{2+}$  ions; The scale bar is 3.0 cm. (b) Electromechanical sensing function. (c) and (d) Antibacterial function of DSI-skin with 4.0%  $Zn^{2+}$  ions; (e) Self-healing capacity of DSI-skin with 2.0%  $Zn^{2+}$  ions; The scale bar is 1.0 cm, respectively. (f) Anti-freezing ability of DSI-skin with 4.0%  $Zn^{2+}$  ions; The scale bars are 1.5 cm and 2.0 cm, respectively.

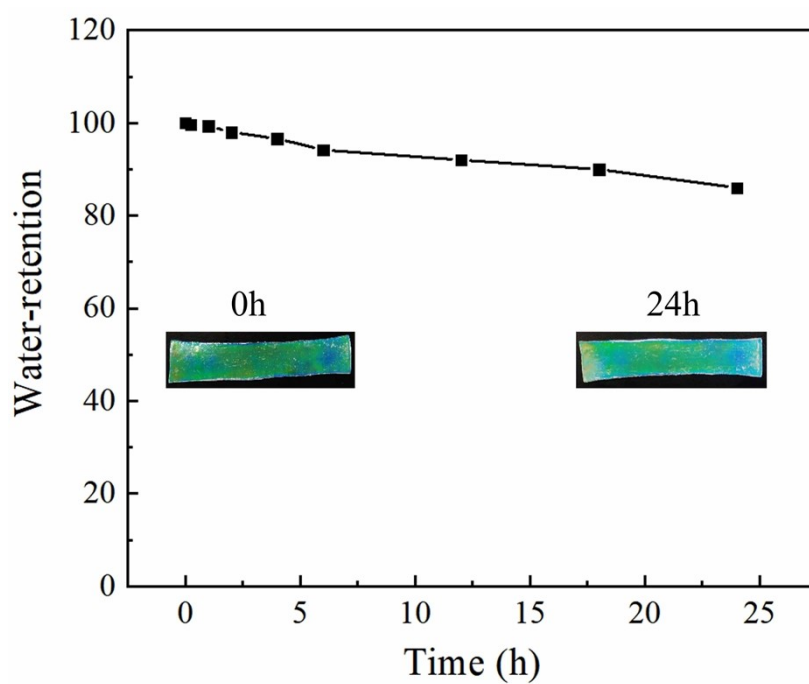


**Figure S13.** Water-retention of DSI-skin under constant temperature (25 °C) and relative humidity (40%) conditions.

From Figure S13, it can be seen that DSI-skin lost only  $\approx 10\%$  of the initial water content after storage for 24h, which barely affect the stability of performances of DSI-skin.

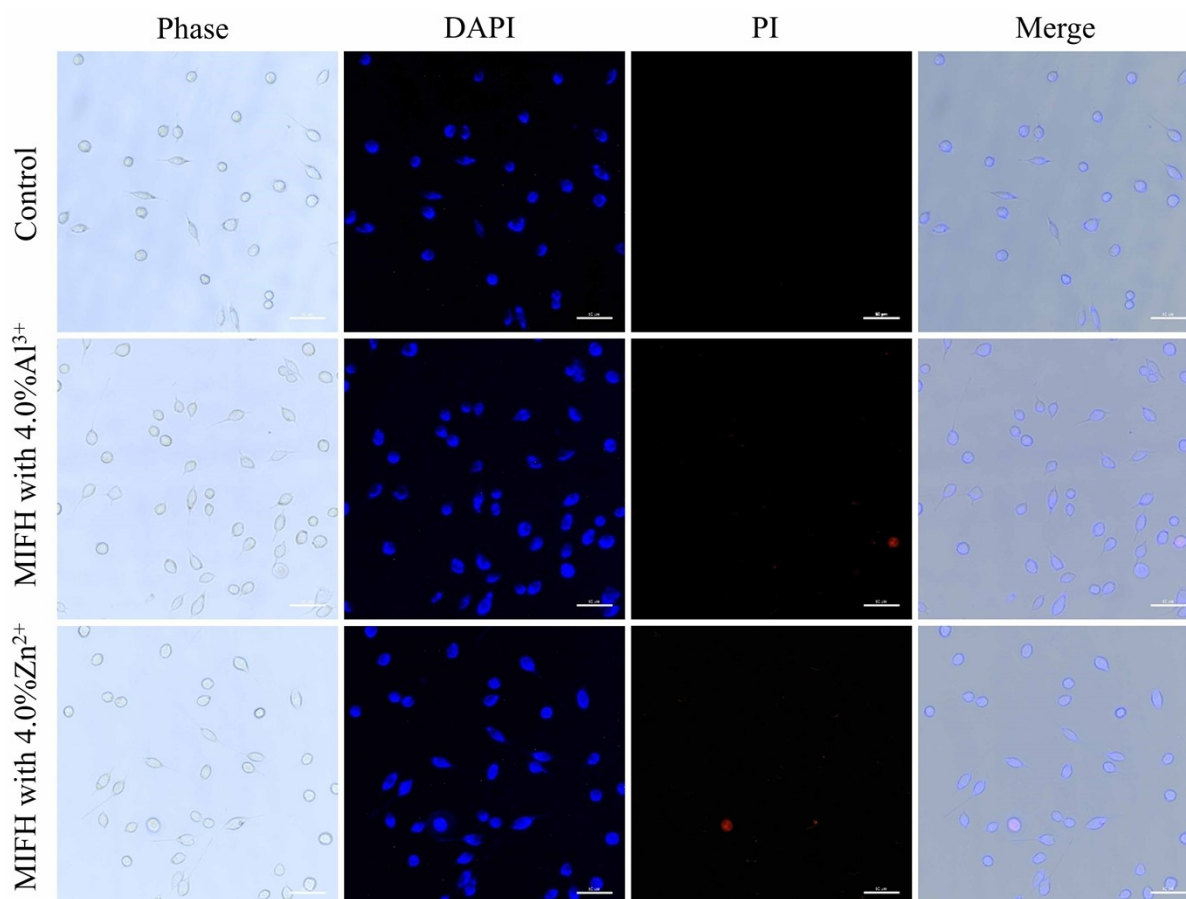


**Figure S14.** Bright field, fluorescence, and merged images of L929 incubated with MIFH with 4.0%  $\text{Al}^{3+}$  ions and 4.0%  $\text{Zn}^{2+}$  ions and stained with DAPI/PI.

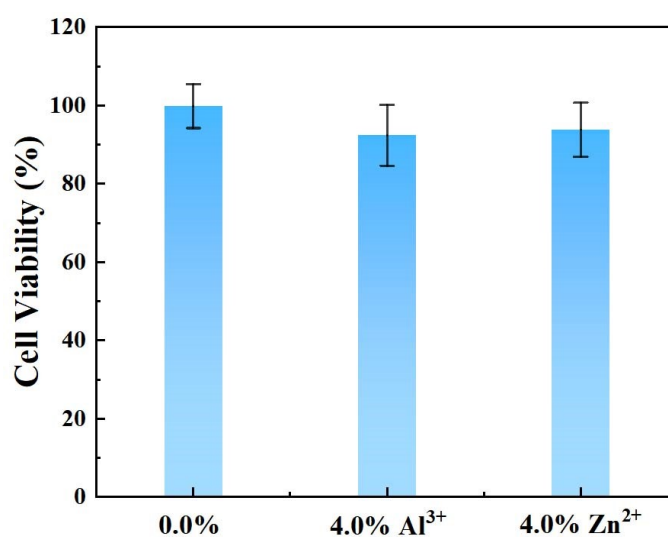


**Figure S15.** Cytotoxicity of the extracts of MIFH (not add ions, 4.0%  $\text{Al}^{3+}$  and 4.0%  $\text{Zn}^{2+}$  ions) against the L929 cell line after incubating for 24 h.

Figure S14 shows that the number of live cells decreased slightly compared to the control group after adding the extracts of our MIFH hydrogel with 4.0%  $\text{Al}^{3+}$  ions or 4.0%  $\text{Zn}^{2+}$  ions.

The cell viability of mouse fibroblasts (L929s) maintained above 90% (4.0% Al<sup>3+</sup> ions: 92.4%; 4.0% Zn<sup>2+</sup> ions: 93.8%) for all the experiment groups, as shown in Figure S15. Because of forming metal coordination bonds between Al<sup>3+</sup>/Zn<sup>2+</sup> ion and carboxylate group, the Al<sup>3+</sup>/Zn<sup>2+</sup> ions are immobilized in the matrix of MIFH hydrogel, which will tremendously reduce the cytotoxicity of metal ions (Adv. Funct. Mater. 2020, 30, 1904156; Chem. Eng. J. 2019, 370, 1228; ACS Appl. Mater. Interfaces 2018, 10, 17018). On the basis of these results we conclude that the MIFH hydrogel show a low cytotoxicity toward the L929 cells.



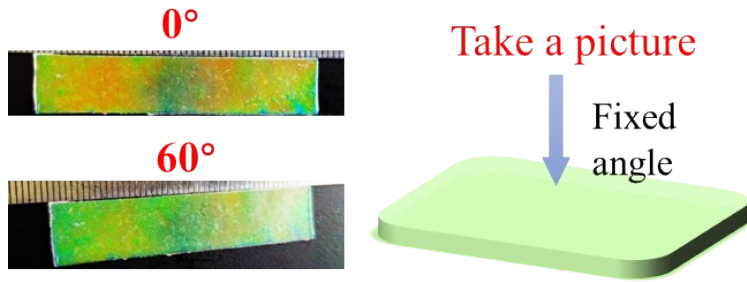


**Figure S16.** Test angle of our mechanochronic sensor.

The angle dependence of color is an inherent property for all photonic crystal materials, which depends on Bragg's Law ( $\lambda = n \times p \times \cos\theta$ ). Our materials are no exception. As shown in Figure S16, it can be seen that the color of our material slightly changes with the viewing angle. In this work, all tests are measured in the vertical direction of the materials for mechanochronic performances, avoiding the error caused by angle. After receiving the external mechanical stimuli, mechanochronic phenomenon is always present at every angle, which does not affect the actual use of the material.

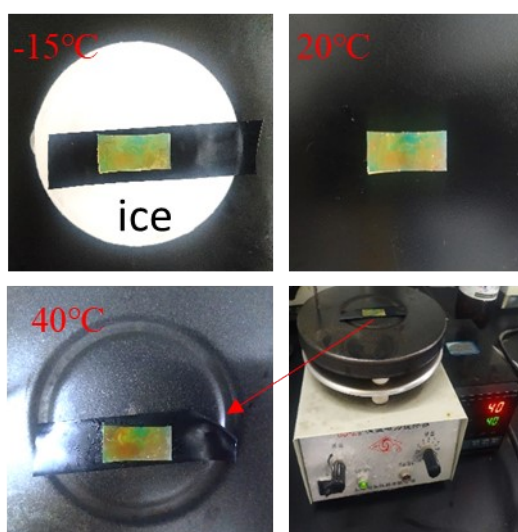


**Figure S17.** Mechanochromic sensing performance with temperature variation.

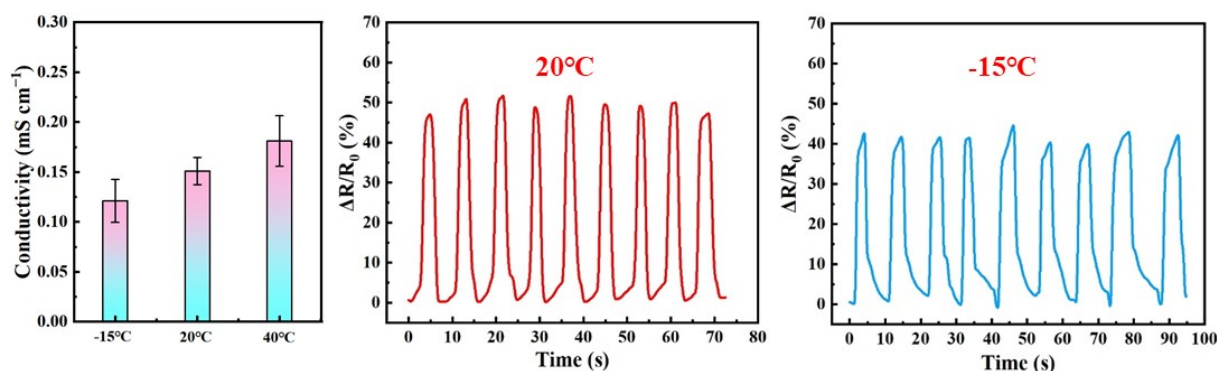


**Figure S18.** Electromechanical sensing performance with temperature variation.

We tested the influence of temperature on the electromechanical and mechanochromic sensing performances, as shown in Figure S17 and S18. It can be seen that the color has a slight red-shift with increasing temperature. This is because that the increase in temperature slightly increases the pitch of lyotropic cholesteric liquid crystals. Simultaneously, an increasing temperature leads to a slight increase in ionic conductivity due to the accelerating ion migration rate. Obviously, the mechanochromic sensing and electromechanical sensing performances can work well at different temperatures, and are almost unaffected by temperature, as shown in Figure S18. In addition, the temperature nearly is a constant value and does not change constantly especially when the material is used as ionic skin. Therefore, the temperature does not cause data errors in normal use.

### 3. Supporting Tables

**Table S1.** Mechanical properties of the current structure color materials and artificial skins.

Ref.	Type	Main constituents	Tensile strength	Elongation
<b>This work</b>	<b>Photonic crystal ionic hydrogel</b>	<b>H-HPC and AlCl<sub>3</sub></b>	<b>200 kPa</b>	<b>≈ 200%</b>
1	Photonic crystal hydrogel	BAS, GelMA and SiO <sub>2</sub>	≈ 2.5 kPa	≈ 33%
2	Photonic polymer	PDMS and CLCE	≈ 400 kPa	40%
3	Photonic crystal hydrogel	PEG and SiO <sub>2</sub> photonic crystals	80 kPa	≈ 175%
4	Photonic crystal hydrogel	Gels and SiO <sub>2</sub> photonic crystals	400 kPa	80%
5	Photonic crystal hydrogel	AAM, HEMA and PS photonic crystals	500 kPa	≈ 120%
6	Photonic crystal hydrogel	Gels, PEG and SiO <sub>2</sub> photonic crystals	≈ 300 kPa	≈ 33%
7	Photonic crystal ionic hydrogel	Surfactant and AAM	≈ 8 kPa	≈ 250%
8	Photonic crystal hydrogel	PEGDA, PDA and inverse opal scaffold	100 kPa	30%
9	Photonic crystal hydrogel	PU, PDA and inverse opal scaffold	40 kPa	600%
10	Photonic crystal hydrogel	PNIPAM, PEGDA, rGO and inverse opal scaffold	150 kPa	100%

**Table S2.** Summary of the previously reported humidity sensors.

Ref.	Type	Visual signal	Electrical signal	Detection range	Response time
<b>This work</b>	<b>Dual signal of ionic hydrogel</b>	<b>Yes</b>	<b>Yes</b>	<b>30~90% RH</b>	<b>0.5 s</b>
11	Ionic hydrogel	No	Yes	45~60% RH	50 s
12	Conducting polymer	No	Yes	20~70% RH	1~30 s
13	Photonic hydrogel	Yes	No	20~100% RH	>10 min
14	Composite polymer	No	Yes	30~80% RH	148 s
15	Photonic hydrogel	Yes	No	20~90% RH	2 s
16	Dielectric elastomer	No	Yes	30~90% RH	20~50 s
17	Metal composite	No	Yes	11~97% RH	110 s
18	Metal composite	No	Yes	11~93% RH	24 s
19	Composite polymer	Yes	No	0~100% RH	0.5 s
20	Photonic crystal film	Yes	No	30~100% RH	15 min
4	Photonic crystal film	Yes	No	45~100% RH	1 h
21	Photonic crystal film	Yes	No	30~100% RH	1 h

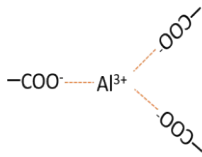
**Table S3.** Comparison between DSI-skins and the previously reported ion skins, photonic sensors or ionic hydrogels in terms of visual signal, electrical signal, antibacterial, self-healing, and anti-freezing functions.

<b>Ref.</b>	<b>Visual signal</b>	<b>Electrical signal</b>	<b>Antibacterial function</b>	<b>Self-healing function</b>	<b>Anti-freezing function</b>
<b>This work</b>	<b>Yes</b>	<b>Ionic conduction</b>	<b>Yes</b>	<b>Yes</b>	<b>Yes</b>
8,22,23	Yes	Electron conduction	No	Yes	No
9,10, 24-26	Yes	Electron conduction	No	No	No
27	Yes	No	Yes	Yes	No
1,7,28	Yes	No	No	Yes	No
29	No	Ionic conduction	Yes	No	Yes
30	No	Ionic conduction	Yes	Yes	No
31	No	Ionic conduction	No	Yes	No
32,33	No	Ionic conduction	No	No	Yes
34	No	Ionic conduction	Yes	No	No
35	No	No	Yes	Yes	No

**Table S4.** Performances of our DSI-skin sensor compared with the previous studies regarding multifunctional hydrogel sensors.

Ref.	Electromechanical sensing	Mechanochromic sensing	Humidity sensing	Antibacterial function	Self-healing function	Anti-freezing function	Mechanical property
<b>This work</b>	<b>GF: 4.90; Sensitivity: 3.14 kPa<sup>-1</sup>; Response time: 363 ms</b>	<b>Visual signal observed by naked eye; Blue to red (426~641 nm)</b>	<b>Dual-signal responses; Response time: 500 ms</b>	<b>Log reduction: &gt;3.43</b>	<b>Efficiency: 85.0%</b>	<b>-15 °C</b>	<b>Tensile strength: 200 kPa; Elongation: 200%</b>
ACS Appl. Mater. Interfaces 2020, 12, 27545	GF: 1.29; Response time: 200 ms	No (not have)	No	No	No	No	800 kPa; 290%
ACS Appl. Mater. Interfaces 2020, 12, 6442	GF: 1.6; Sensitivity: 0.013 kPa <sup>-1</sup> ; Response time: 171 ms	No	No	No	No	No	70 kPa; 900%
ACS Appl. Mater. Interfaces, 2020, 12, 6797	Response time: 1 s	No	No	No	97%	No	3000 kPa; 320%
ACS Appl. Mater. Interfaces, 2019, 11, 16765	GF: 1.8	No	No	No	No	No	1600 kPa; 220%
Adv. Sci., 2017, 4, 1600404	Response time: 400 ms	No	Only electrical signal	No	No	No	No
Chem. Eng. J., 2020, 394, 124941	No	No	No	No	95%	No	11 kPa; 4500%
Nat. commun., 2019, 10, 536	No	No	No	No	85%	No	60 kPa; 1200%

**Table S5.** Novelities of our work compared with the other flexible sensors with electrical and visual dual-sensing functions.

Function system	Other flexible sensors with electrical and visual dual-sensing functions in Table S1 and Figure 8	This work	Our virtues and novelties
Conduction	Electron and hole transduction (carbon nanotube, graphene)	<b>Ionic transduction (Al<sup>3+</sup>/Zn<sup>2+</sup> ions)</b>	<b>Our work is ionic transduction similar to biological system, which possesses inexpensive cost, good biocompatibility,</b> and no agglomerations compared with electron transduction materials.
Color tuning	SiO <sub>2</sub> particle size and concentration of structural color material (The color tuning is time-consuming.)	<b>Al<sup>3+</sup> ions content</b> (The color tuning is very easy. The addition amount of Al <sup>3+</sup> is small. (4.0% Al <sup>3+</sup> : red; 2.0% Al <sup>3+</sup> : green; 0.0% Al <sup>3+</sup> : blue;) (426~640nm)	<b>The color tuning of structural color material by Al<sup>3+</sup> ions and its mechanism have not been reported yet.</b> The mode is facile and convenient. The detailed mechanism is introduced in this paper, Page 3.
Pressure sensing	Color signals derive from structural color material, and electrical signals come from electron transduction material.	Color signals derive from synergistic effect of H-HPC and Al <sup>3+</sup> ions, and electrical signals come from Al <sup>3+</sup> ions.	<b>Our work realizes ionic conduction, visual color signals, color tuning, together with antibacterial, self-healing, and anti-freezing functions by the synergistic effect of H-HPC and Al<sup>3+</sup> ions.</b> However, the dual signals of the other flexible sensors simply rely on the mixture of structural color material and conductive material, which are not synergistic effects.
Strain sensing	Color signals derive from structural color material, and electrical signals come from electron transduction material.	Color signals derive from synergistic effect of H-HPC and Al <sup>3+</sup> ions, and electrical signals come from Al <sup>3+</sup> ions.	<b>Our work realizes ionic conduction, visual color signals, color tuning, together with antibacterial, self-healing, and anti-freezing functions by the synergistic effect of H-HPC and Al<sup>3+</sup> ions.</b> However, the dual signals of the other flexible sensors simply rely on the mixture of structural color material and conductive material, which are not synergistic effects.
Humidity sensing	No	<b>The synergistic effect of H-HPC and Al<sup>3+</sup> ions</b>	<b>In this work, humidity is detected by a dual-signal response using structural color and ion resistance for the first time, as shown in Table S2.</b> H-HPC not only can form bright structural color, but also has a good hygroscopic ability, while Al <sup>3+</sup> ions can offer a sensitive digital signal. The synergistic effect of H-HPC and Al <sup>3+</sup> ions endows the material an excellent humidity sensing.
Self-healing function	No	 <p>(Dynamic coordination bonds)</p>	Our dual-sensing ionic skin also has a nice self-repair ability derived from the dynamic coordination bonds between the carboxyl groups and Al <sup>3+</sup> ions, <b>which can extend the life of the material and reduce e-waste pollution.</b>
Antibacterial function	No	<b>Al<sup>3+</sup> ions</b>	Due to the introduction of Al <sup>3+</sup> ions, our dual-sensing ionic skin also can be endowed with outstanding antibacterial function, <b>which prevents the invasion of bacteria and protects the health of the human body.</b>
Anti-freezing function	No	<b>The synergistic effect of Al<sup>3+</sup> ions and H-HPC</b> (Reduce material freezing point)	Owing to the synergistic effect of Al <sup>3+</sup> ions and H-HPC, our dual-sensing ionic skin also can be endowed with anti-freezing function, <b>which allows the material to function well in extreme environments.</b>

## Supporting References

- [1] F. F. Z. Y. Chen, Z. Zhao, H. Wang, L. Shang, Z. Z. Gua, Y. J. Zhao, *Proc. Natl. Acad. Sci.* **2017**, *114*, 5900.
- [2] P. Zhang, X. Y. Shi, A. H. J. Schenning, G. F. Zhou, L. T. Haan, *Adv. Mater. Interfaces* **2020**, *7*, 1901878.
- [3] Y. X. Dong, A. Bazrafshan, A. Pokutta, F. Sulejmani, W. Sun, J. D. Combs, K. C. Clarke, K. Salaita, *ACS Nano* **2019**, *13*, 9918.
- [4] F. Hu, L. Zhang, W. Z. Liu, X. X. Guo, L. Shi, X. Y. Liu, *ACS Appl. Mater. Interfaces* **2019**, *11*, 15195.
- [5] J. Y. Huang, M. Y. Chen, Y. Q. Zhou, Y. Li, Y. Q. Hu, *Int. J. Biol. Macromol.* **2020**, *162*, 1250.
- [6] Z. Y. Chen, J. D. Wu, Y. Wang, C. M. Shao, J. J. Chi, Z. Y. Li, X. H. Wang, Y. J. Zhao, *Small* **2019**, *15*, 1903104.
- [7] Y. Wang, L. Shang, G. Chen, L. Y. Sun, X. X. Zhang, Y. J. Zhao, *Sci. Adv.* **2020**, *6*, eaax8258.
- [8] Y. Wang, Y. R. Yu, J. H. Guo, Z. H. Zhang, X. X. Zhang, Y. J. Zhao, *Adv. Funct. Mater.* **2020**, *30*, 2000151.
- [9] Y. P. Wang, X. F. Cao, J. Cheng, B. Yao, Y. Zhao, S. Wu, B. Z. Ju, S. F. Zhang, X. M. He, W. B. Niu, *ACS Nano* **2021**, *15*, 3509.
- [10] Y. Wang, J. H. Guo, L. Y. Sun, H. X. Chen, Y. J. Zhao, *Chem. Eng. J.* **2021**, *415*, 128978.
- [11] H. T. Yu, Y. T. Guo, C. Yao, D. Perepichkab, H. Meng, *J. Mater. Chem. C* **2016**, *4*, 11055.
- [12] C. Steffens, A. N. Brezolin, J. Steffens, *Scanning* **2018**, *2018*, 4782685.
- [13] Z. Wang, M. Xue, H. Zhang, Z. H. Meng, K. J. Shea, L. L. Qiu, T. T. Jia, T. S. Xie, *RSC Adv.* **2018**, *8*, 9963.



- [14] A. Hou, H. H. Chen, C. W. Zheng, K. L. Xie, A. Q. Gao, *ACS Nano* **2020**, *14*, 7380.
- [15] W. Jeong, J. Song, J. Bae, K. R. Nandanapalli, S. Lee, *ACS Appl. Mater. Interfaces* **2019**, *11*, 44758.
- [16] M. B. Sobhanimatin, S. Pourmahdian, M. M. Tehranchi, *Mater. Today Commun.* **2021**, *26*, 101997.
- [17] M. Momtaz, J. Chen, *Sens. Actuators, B* **2021**, *329*, 129268.
- [18] T. Chandrasekhar, N. Sasidhar, B. Chethan, Y. T. Ravikiran, *AIP Publishing LLC* **2020**, *2274*, 020012.
- [19] S. Kunchakara, A. Ratan, M. Dutt, J. Shah, R. K. Kotnala, V. Singh, *J. Phys. Chem. Solids* **2020**, *145*, 109531.
- [20] K. Yao, Q. J. Meng, V. Bulone, Q. Zhou, *Adv. Mater.* **2017**, *29*, 1701323.
- [21] H. H. Chen, A. Q. Hou, C. W. Zheng, J. Tang, K. L. Xie, A. Q. Gao, *ACS Appl. Mater. Interfaces* **2020**, *12*, 24505.
- [22] W. B. Niu, X. F. Cao, Y. P. Wang, B. W. Yao, Y. S. Zhao, J. Cheng, S. L. Wu, S.F. Zhang, X. M. He, *Adv. Funct. Mater.* **2021**, <https://doi.org/10.1002/adfm.202009017>.
- [23] J. Zhang, J. J. Zhang, Y. T. Ou, Y. P. Qin, H. L. Wen, W. L. Dong, R. Wang, S. Chen, Z. Y. Yu, *Small* **2021**, *17*, 2007426.
- [24] H. Xu, M. K. Zhang, Y. F. Lu, J. J. Li, S. J. Ge, Z. Z. Gu, *Adv. Mater. Technol.* **2020**, *5*, 1901056.
- [25] Y. P. Wang, W. B. Niu, C. Y. Lo, Y. S. Zhao, X. M. He, G. R. Zhang, S. L. Wu, B. Z. Ju, S. F. Zhang, *Adv. Funct. Mater.* **2020**, *30*, 2000356.
- [26] Z. H. Zhang, Z. Y. Chen, Y. Wang, Y. J. Zhao, *Proc. Natl. Acad. Sci.* **2020**, *117*, 18310.
- [27] S. X. Bao, J. T. Gao, T. F. Xu, N. Li, W. X. Chen, W. Y. Lu, *ACS Appl. Mater. Interfaces* **2017**, *9*, 38901.
- [28] Z. Y. Chen, J. D. Wu, Y. Wang, C. M. Shao, J. J. Chi, Z. Y. Li, X. H. Wang, Y. J. Zhao,

*Small* **2019**, *15*, 1903104.

[29] S. X. Bao, J. T. Gao, T. F. Xu, N. Li, W. X. Chen, W. Y. Lu, *Chem. Eng. J.* **2021**, *411*, 128470.

[30] S. H. Li, H. Y. Pan, Y. T. Wang, J. Q. Sun, *J. Mater. Chem. A* **2020**, *8*, 3667.

[31] Z. Y. Lei, P. Y. Wu, *Nat. Commun.* **2018**, *9*, 1134.

[32] J. Wen, J. Tang, H. M. Ning, N. Hu, Y. Y. Zhu, Y. K. Gong, C. H. Xu, Q. N. Zhao, X.P. Jiang, X. L. Hu, L. Lei, D. Wu, T. Huang, *Adv. Funct. Mater.* **2021**, <https://doi.org/10.1002/adfm.202011176>.

[33] Z. R. He, W. Z. Yuan, *ACS Appl. Mater. Interfaces* **2021**, *13*, 1474.

[34] X. Lin, Y. X. Mao, P. Li, Y. J. Bai, T. Chen, K. Wu, D. D. Chen, H. L. Yang, L. Yang, *Adv. Sci.* **2021**, <https://doi.org/10.1002/advs.202004627>.

[35] J. Z. Pan, Y. Jin, S. Q. Lai, L. J. Shi, W. H. Fan, Y. C. Shen, *Chem. Eng. J.* **2019**, *370*, 1228.

## 4. Supporting Movie

**Supporting MovieS1-9:** See attachment MovieS1-9.zip